Extreme THz fields from two-color filamentation of midinfrared laser pulses

Vladimir Yu. Fedorov[1,2,*] and Stelios Tzortzakis[1,3,4,†]

[1]*Science Program, Texas A&M University at Qatar, P.O. Box 23874, Doha, Qatar*

[2]*P. N. Lebedev Physical Institute of the Russian Academy of Sciences, 53 Leninskiy Prospekt, 119991 Moscow, Russia*

[3]*Institute of Electronic Structure and Laser (IESL), Foundation for Research and Technology - Hellas (FORTH), P.O. Box 1527, GR-71110 Heraklion, Greece*

[4]*Materials Science and Technology Department, University of Crete, 71003 Heraklion, Greece*

(Received 7 August 2017; published 21 June 2018)

Nonlinear THz photonics is probably the last frontier of nonlinear optics. The strength of both the electric and the magnetic fields of these ultrashort low-frequency light bunches opens the way to exciting science and applications. Progress in the field though is slow because of the deficiency in suitable sources. Here we show that two-color filamentation of midinfrared 3.9 μm laser pulses allows one to generate single-cycle THz pulses with multimillijoule energies and record conversion efficiencies. Moreover, the focused THz peak electric and magnetic fields reach values of GV/cm and kT, respectively, exceeding by far any available quasi-dc field source today. These fields enable extreme field science, including into other, relativistic phenomena. In addition, we elucidate the origin of this high efficiency, which is made up of several factors, including a mechanism where the harmonics produced by the midinfrared pulses strongly contribute to the field symmetry breaking and enhance the THz generation.

DOI: 10.1103/PhysRevA.97.063842

I. INTRODUCTION

The terahertz (THz) frequency range (0.1–10.0 THz) is a part of the electromagnetic spectrum, located at the junction between the microwave (high-frequency electronics) and optical (photonics) frequencies. For many reasons, THz frequencies have attracted a lot of interest in recent years [1,2]. For instance, THz radiation penetrates through a variety of nonconducting materials such as clothing, paper, wood, masonry, plastic, and ceramics. But unlike x rays, THz radiation is not an ionizing radiation and does not damage test materials, which opens great opportunities for its application in industrial quality control, homeland security, and medical diagnostics and treatment.

Although the THz frequency range has very rich scientific and technological potential, it remains underexplored due to the lack of intense THz sources and sensitive THz detectors. The progressive appearance of suitable bright THz sources opens a new era for studies of extreme THz field-matter interactions, nonlinear THz spectroscopy, and imaging. To date, there are two major techniques for the generation of intense THz pulses on tabletop setups [3,4]: optical rectification in nonlinear crystals [5–8] and two-color filamentation (photoionization of gases by dual-frequency laser fields) [9–11]. Optical rectification has THz conversion efficiencies (ratio of generated THz energy to energy of input laser pulse) that can reach 3.7% [5]. Nevertheless, the spectral bandwidth of these sources is limited to frequencies below 5 THz and the generated THz pulses energies are also limited because of the damage threshold of crystals, with the highest energy reported to date reaching 0.9 mJ [6]. In turn, two-color filamentation presents lower THz conversion efficiencies ($\sim$0.01%) and produces less intense THz pulses with energies up to 30 μJ in gases [9–11] and up to 80 μJ in liquids [12]. However, THz pulses generated by two-color filamentation have much larger spectral bandwidths (>50 THz) and can be generated at remote distances [13–16], which allows one to overcome a number of THz propagation issues such as high absorption in atmospheric water vapor and diffraction.

Currently, most experiments on two-color filamentation have been conducted using Ti:sapphire laser sources with a central wavelength around 0.8 μm and their second harmonic. A study using longer wavelengths, in the near infrared, showed an enhancement of THz conversion efficiency with increasing pump wavelength, but only up to 1.8 μm, while beyond this point the efficiency dropped again [17]. Also, a theoretical study showed stronger THz generation compared to 0.8 μm using single-color midinfrared pulses with particle in cell (PIC) simulations, not considering though nonlinear propagation effects [18]. Recently though, filamentation of midinfrared (mid-IR) laser pulses with a 3.9 μm central wavelength was demonstrated experimentally [19]. The subsequent experimental and theoretical studies revealed that compared to 0.8 μm laser pulses, filaments produced by 3.9 μm are longer with wider plasma channels and the generated supercontinuum is extremely broad, ranging up to harmonics of 15th order [19–24].

In this work, we study numerically the generation of THz radiation by two-color filamentation of 3.9 μm laser pulses. We show that compared to 0.8 μm pulses, the THz conversion efficiency in mid-IR filaments is two orders of magnitude higher, the energy of generated THz pulses reaches the multimillijoule level, and the strength of THz fields can reach the GV/cm range. Thus, two-color filamentation of mid-IR laser pulses emerges as the ultimate source for extreme THz science since it allows one to generate THz radiation with unprecedented

*v.y.fedorov@gmail.com

†stzortz@iesl.forth.gr

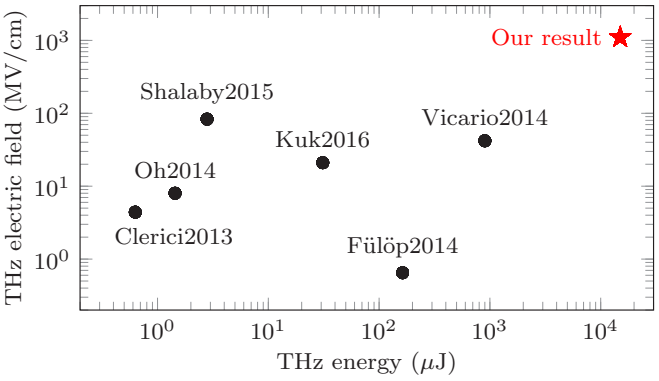

FIG. 1. Comparison of energy and electric field of our source with present state-of-the-art tabletop THz sources: Clerici2013 [17], Oh2014 [10], Shalaby2015 [8], Kuk2016 [11], Fülöp2014 [7], and Vicario2014 [6].

efficiency and extremely high energy that largely overcomes all other approaches (see comparison of our result with present state-of-the-art tabletop THz sources in Fig. 1), while energy scaling does not suffer from undesired effects such as damage of crystals in the optical rectification.

II. MODEL

To simulate the two-color filamentation of mid-IR laser pulses in air, we use the unidirectional pulse propagation equation (UPPE) [25,26] coupled with the kinetic equation for plasma concentration [27] (see the Appendix). This model takes into account nonparaxial propagation of polychromatic fields without any kind of envelope approximations. It includes dispersion of all orders, cubic Kerr nonlinearity, defocusing in plasma, inverse Bremsstrahlung, photoionization with corresponding energy losses, and avalanche ionization. We use a realistic dispersion model of dry atmospheric air (zero relative humidity) that takes into account spectral lines of N_2, O_2, and CO_2 gases from the HITRAN database [28].

Our initial condition for the UPPE equation is the following two-color field E:

$$E = \exp\left(-\frac{r^2}{2a_0^2} - \frac{t^2}{2\tau_0^2}\right)[E_1\cos(\omega_0 t) + E_2\cos(2\omega_0 t)],$$

where $r^2 = x^2 + y^2$, $a_0 = 4/2\sqrt{\ln 2}$ mm is the beam size (4 mm FWHM), $\tau_0 = 100/2\sqrt{\ln 2}$ fs is the pulse duration (100 fs FWHM), and ω_0 is the central frequency, while E_1 and E_2 are the amplitudes of fundamental and second harmonic pulses, respectively. The initial pulse is focused by a lens with a focal distance $z_f = 200$ mm. To simulate the focusing, we multiplied each Fourier harmonic of the field E by a factor $\exp[-i(\omega/c_0)r^2/(2z_f)]$, where ω is the frequency of the corresponding harmonic and c_0 is the speed of light in vacuum. In our simulations, the central wavelength λ_0 of the fundamental pulse is equal to 3.9 μm. Also, in order to have a reference for comparison, we simulated two-color filamentation of the same laser pulse but with $\lambda_0 = 0.8$ μm. The energy W of the initial two-color pulse is equal to 29 mJ for $\lambda_0 = 3.9$ μm and 1.23 mJ for $\lambda_0 = 0.8$ μm. For both cases, the fundamental and second harmonic pulses hold, respectively, 95% and 5% of this energy. The energy W for each wavelength was chosen in such a way that the power of the corresponding single-color pulse at wavelength λ_0 is equal, in both cases, to $1.2P_{cr}$, where P_{cr} is the critical power of self-focusing in air at this wavelength.

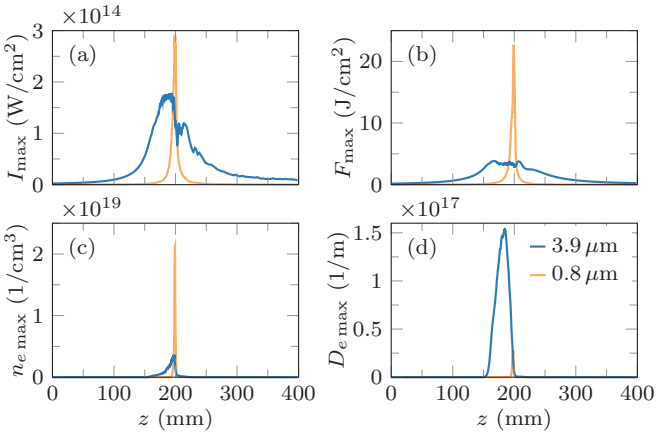

FIG. 2. (a) Peak intensity $I_{\max}$, (b) peak fluence $F_{\max}$, (c) peak plasma concentration $n_{e\max}$, and (d) plasma concentration integrated over radius, $D_{e\max}$, vs propagation distance z for the 3.9 μm [blue (dark-gray) line] and the 0.8 μm [orange (light-gray) line] two-color laser pulses.

III. RESULTS

Using the above model, we numerically simulated the two-color filamentation of 3.9 μm and 0.8 μm pulses in air. Figure 2 shows the dependence of several filamentation integral parameters on propagation distance for both wavelengths. One can see that the peak intensity, peak fluence (intensity integrated over time), and peak plasma concentration in the case of a 3.9 μm pulse are several times lower than for the 0.8 μm pulse. However, the filament produced by the 3.9 μm pulse is about three times longer. Moreover, much higher integrated over radius plasma concentration shows that the plasma channel produced by the 3.9 μm pulse is considerably wider compared to the 0.8 μm pulse.

Figure 3 shows the dependence of integrated power spectrum S on propagation distance z and frequency f for the two wavelengths. One can see that filamentation of the 3.9 μm two-color pulse is accompanied by the generation of an extremely broad supercontinuum, which includes all even and odd harmonics up to the 15th order (harmonics of higher order lie out of the atmospheric transparency window that ends at $\lambda \approx 0.25$ μm or $f \approx 1200$ THz). However, the most intriguing result is the impressive energy transferred to the THz part of the spectrum with the 3.9 μm pulses compared to the case of 0.8 μm ones. The THz conversion efficiency (for frequencies f lying below 40 THz) for 0.8 μm pulses is 0.06%, while the one for 3.9 μm pulses is 6.7%, which is more than two orders of magnitude higher. Note that this conversion efficiency is the highest reported to date compared to any of the known approaches for THz generation.

Figure 4(a) [blue (dark-gray) line] shows how the energy of the THz pulse generated during two-color filamentation of 3.9 μm pulses depends on the propagation distance z. One

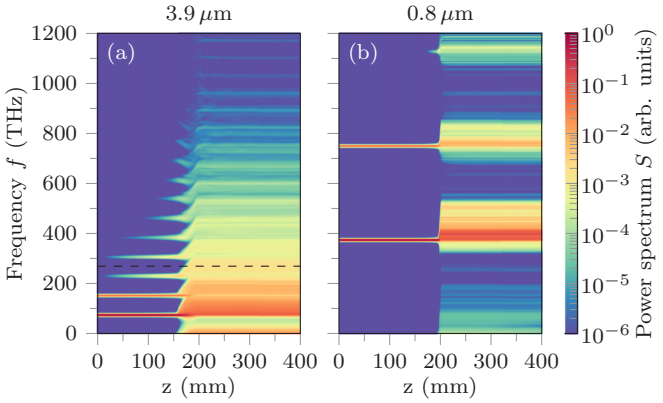

FIG. 3. Dependence of integrated pulse power spectrum S on propagation distance z and frequency f for (a) 3.9 μm and (b) 0.8 μm two-color laser pulses. The black dashed line separates the harmonics of fourth order and higher.

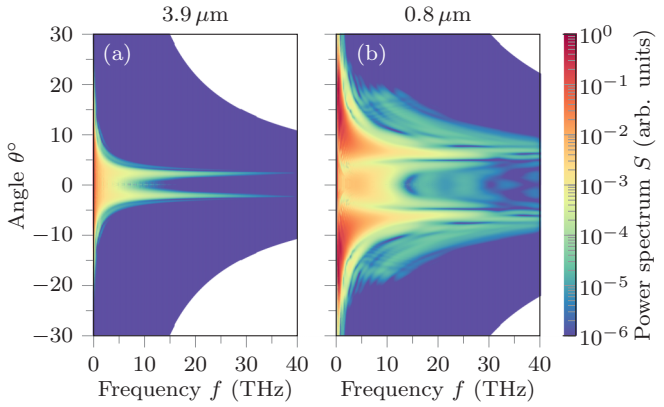

FIG. 5. Dependence of pulse power spectrum S on frequency f and angle θ for (a) 3.9 μm and (b) 0.8 μm two-color laser pulses at distance $z = 220$ mm.

can see that close to the end of the filament ($z \simeq 220$ mm), the energy of the THz pulse reaches almost 2 mJ. Note that the decrease of THz energy at longer propagation distances is purely numerical and is due to losses of the diffracting THz beam in the absorbing boundary layers located at the ends of the numerical grid. In turn, the peak THz energy generated by 0.8 μm pulses is only about 0.8 μJ. In other words, the THz pulse generated by the 3.9 μm pulse is 2500 times (three orders of magnitude) more energetic than the one generated by 0.8 μm pulses.

Figure 4(b) [blue (dark-gray) line] shows the on-axis THz electric field generated by 3.9 μm pulses at a distance $z = 190$ mm (in the middle of the filament). One can see that the field strength (the amplitude from minimum to maximum of the field) of the generated THz pulse reaches 56 MV/cm, which exceeds the field strengths obtained in the most efficient experiments with optical rectification [6].

Figure 5 shows the angularly resolved frequency spectrum of the THz pulse generated during two-color filamentation of 3.9 μm and 0.8 μm pulses. One can see that in both cases, the THz radiation is emitted into a cone, where higher frequencies propagate at smaller angles. Also, we see that on average, the angle of the THz emission cone is smaller in the case of $\lambda_0 = 3.9$ μm ($\sim 7^\circ$ for 0.8 μm and $\sim 2^\circ$ for 3.9 μm pulses). Thus, an extra advantage of THz radiation produced during two-color filamentation of 3.9 μm is its better directionality compared to the case of 0.8 μm pulses.

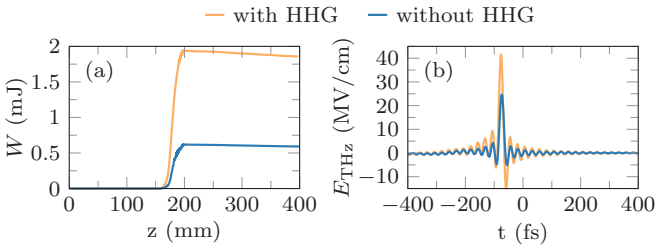

FIG. 4. (a) Energy of THz pulse W vs propagation distance z. (b) THz electric field vs time t at $z = 190$ mm. THz pulses are generated during two-color filamentation of 3.9 μm pulses in the case of air with [orange (light-gray) line] or without [blue (dark-gray) line] high harmonics generation.

IV. DISCUSSION

As we have already seen, two-color filamentation of mid-IR laser pulses allows one to generate THz pulses of very high energy and field strength. High efficiency of THz generation by mid-IR two-color pulses is made up of several factors. Maybe the most intriguing of them is related to the highly efficient generation of high harmonics during mid-IR filamentation. In Fig. 3, we see that the spectrum produced by 3.9 μm pulses consists of all harmonics, both even and odd, up to the 15th order. Thus, filamentation of two-color 3.9 μm pulses is accompanied by the generation of a multiple number of secondary dual-frequency pulses ($2\omega - 4\omega$, $3\omega - 6\omega$, $4\omega - 8\omega$, etc.). Each of these secondary pulses contributes to the field symmetry breaking and supports further THz generation. In order to test this hypothesis, we repeated the simulations of two-color filamentation with 3.9 μm pulses, but during these simulations at each propagation step we filtered out all harmonics of order four and higher (the black dashed line in Fig. 3 shows the boundary of the spectral filter). The energy and the electric field of THz pulses obtained from these simulations are plotted in Fig. 4 [orange (light-gray) lines]. One can see that without higher harmonics, the energy of the generated THz pulse drops down by three times.

In addition, mid-IR laser pulses produce much stronger photocurrents compared to 0.8 μm pulses. This can be seen from the following estimations. The velocity v of a free electron under the action of the Lorentz force produced by a monochromatic field of amplitude A and frequency ω_0 is given by the equation $dv/dt = q_e/m_e A\cos(\omega_0 t)$, where q_e and m_e are the charge and mass of electron, respectively. After integration, we find $v = (q_e/m_e)(A/\omega_0)\sin(\omega_0 t)$ (the initial velocity of free electrons after ionization is assumed to be zero). Therefore, the average electron velocity $\sqrt{v^2} = (q_e/m_e)(A/2\omega_0)$ is proportional to the wavelength $\lambda_0 = 2\pi c_0/w_0$. Thus, the photocurrent $J = q_e v$ produced by 3.9 μm pulses and, as a consequence, the generated THz field are about five times stronger compared to 0.8 μm pulses.

Another factor contributing to the highly efficient THz generation is a smaller walk-off between the fundamental and the second harmonic. According to our dispersion model (see the Appendix), the walk-off between 0.4 μm and 0.8 μm pulses

is 81 fs/m. In turn, the walk-off between 1.95 μm and 3.9 μm pulses is only 1.26 fs/m for air with CO_2 and 3.04 fs/m for air without CO_2. That is, the walk-off for 3.9 μm two-color pulses is at least 20 times less than for 0.8 μm pulses. In turn, keeping in mind the Cherenkov mechanism of THz generation [29], smaller walk-off between the THz and fundamental pulses explains the better directionality of THz radiation in the case of mid-IR pulses (see Fig. 5).

Besides, the THz generation efficiency is higher for 3.9 μm two-color pulses because it produces ~3 times longer plasma channels that contain ~45 times more free electrons (see Fig. 2).

Interestingly, in our studies we did not reveal any effect of CO_2 gas on THz generation efficiency, as one could suggest because of the absorption line near 3.9 μm and the corresponding anomalous dispersion (see the Appendix). For air with and without CO_2, the results of our simulations are so close that it is very hard to see any difference on any of the above figures.

To sum up, the much higher efficiency of THz generation by 3.9 μm two-color pulses compared to 0.8 μm ones can be explained by the extra field symmetry breaking due to higher harmonics, the five-times-stronger photocurrents, the tens-of-times-smaller walk-off between the fundamental and its second harmonic, the three-times-longer plasma channels, and the 45-times-more total free electrons. We must stress though that the contribution of individual physical mechanisms cannot be decoupled, and simple extrapolations for the longer driving laser wavelengths prove to be wrong. This complexity is known to the community, as can be seen for instance in [17], where a decrease was observed in the THz energy for wavelengths longer than 1.8 μm, which is something that cannot be explained by simply scaling the independent physical contributions, such as the ponderomotive force. The physics of the process is significantly more complex and one must appropriately consider the rich spatiotemporal and ionization effects emanating from the long nonlinear propagation and filamentation as we show here.

In addition, we studied how the parameters of the generated THz radiation scale with the input energy W of 3.9 μm two-color pulses. Figure 6(a) shows that the energy of the generated THz pulse growths almost linearly with W, reaching 15 mJ at $W = 232$ mJ. The THz conversion efficiency weakly depends on input energy and is about 7 % [see Fig. 6(b)]. The peak THz electric field strengths obtained for $W = 29$, 58, 116, and 232 mJ are equal to 56, 65, 67, and 77 MV/cm, respectively. Considering the almost linear increase of THz energy with increasing W and taking into account that the width of the THz spectrum remains the same, this rather small growth of the THz field strength suggests that the spatial size of the generated THz pulses increases with W. To verify this, we calculated the fluence distributions (intensities integrated over time) for all THz pulses and estimated their $1/e$ radii a_{THz} using a Gaussian fitting. As a result, we obtained $a_{\mathrm{THz}} = 0.5$, 0.77, 1.72, and 2.2 mm for the corresponding input energies $W = 29, 58, 116$, and 232 mJ. Thus, the growth of THz energy with the increase of input laser energy happens mainly due to the increase of THz beam size.

Although the obtained THz field strengths already exceed the highest reported values, one can reach even higher values

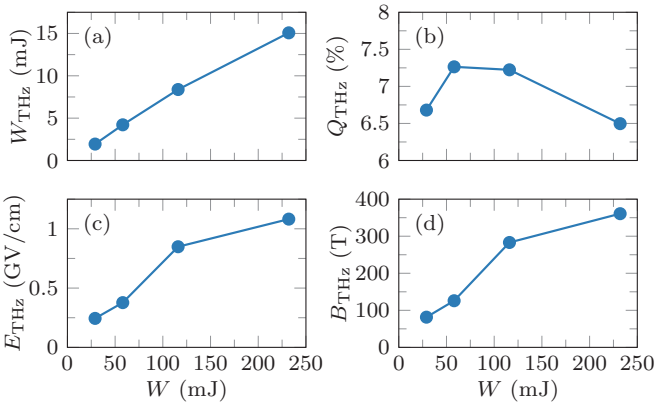

FIG. 6. (a) THz pulse energy W_{THz}, (b) THz conversion efficiency Q_{THz}, (c) estimated peak electric E_{THz}, and (d) magnetic field B_{THz} of focused THz pulse vs input energy W of 3.9 μm two-color laser pulses.

when focusing the corresponding THz beams. As a simple estimate, we recall that for Gaussian beams, the field at the focus of a lens with focal distance f is L_d/f times higher than the initial one. Here, $L_d = 2\pi f_0/c_0 a_0^2$ is the diffraction length, where f_0 is the central frequency and a_0 is the $1/e$ beam radius. We apply this estimate for our THz pulses using the previously calculated radii a_{THz} and $f_0 = 8$ THz. This central frequency corresponds to the center of mass of the THz power spectrum (we found that f_0 does not change with W). Figure 6(c) shows that the estimated THz field strengths E_{THz} in the focus of a 1″ off-axis parabolic mirror ($f = 25.4$ mm) reach the GV/cm level (1.1 GV/cm for $W = 232$ mJ). In turn, the corresponding magnetic fields $B_{\mathrm{THz}} = E_{\mathrm{THz}}/c_0$ reach several hundreds of tesla [see Fig. 6(d)].

Note that the above estimates are quite relaxed, for the $W = 232$ mJ case, for example, the above focusing conditions produce a THz focal waist that is about 2.8 times the central THz wavelength. This means that one could achieve even stronger focusing, such as, for instance, in [8]. This in turn would result in magnetic fields that go beyond the kT regime, exceeding any laboratory-produced quasi-dc magnetic field reported to date by any means.

V. CONCLUSIONS

In conclusion, we numerically simulated two-color filamentation of 3.9 μm laser pulses in realistic atmospheric air. We have shown that compared to the case of 0.8 μm pulses, THz generation efficiency by 3.9 μm two-color pulses is two orders of magnitude higher. The energy of THz radiation generated by 3.9 μm two-color pulses reaches the multimillijoule level, the THz electric field strengths can go beyond the GV/cm level, and the magnetic fields can reach kT. Such high THz efficiency and energy of THz pulses generated by mid-IR pulses is the result of several factors, including a mechanism where generated high harmonics contribute to the field symmetry breaking. The other factors are stronger photocurrents, negligible walk-offs between harmonics, and longer and wider plasma channels. As a result, we have shown that two-color filamentation of mid-IR laser pulses, being a source of extremely bright THz radiation,

can open the way for future studies of extreme THz field-matter interactions, nonlinear THz spectroscopy, and imaging.

ACKNOWLEDGMENTS

This work was supported by the National Priorities Research Program Grant No. NPRP9-383-1-083 from the Qatar National Research Fund (member of The Qatar Foundation) and the European Union Horizon 2020 Laserlab Europe (Grant No. EC-GA 654148).

APPENDIX: DETAILS OF THE MODEL USED IN THE SIMULATIONS

In our simulations, we use the unidirectional pulse propagation equation (UPPE) [25–27] given by

$$\frac{\partial \hat{E}}{\partial z} = ik_z\hat{E} + i\frac{\mu_0\mu\omega^2}{2k_z}\hat{N}, \tag{A1}$$

where $\hat{E}(k_x,k_y,\omega,z)$ is the spatiotemporal spectrum of the laser pulse, $\hat{N}(k_x,k_y,\omega,z)$ represents the nonlinear response of the medium, $k_z(k_x,k_y,\omega) = [k^2(w) - k_x^2 - k_y^2]^{1/2}$ is the propagation constant, k_x, k_y, and ω are the spatial and temporal angular frequencies, and μ_0 and μ are the vacuum and medium permeabilities, respectively. The nonlinear response takes into account the third-order nonlinear polarization P_{nl}, the current of free electrons J_f, and the current that is responsible for ionization losses J_a:

$$\hat{N} = \hat{P}_{nl} + \frac{i}{\omega}(\hat{J}_f + \hat{J}_a), \tag{A2}$$

with

$$\hat{P}_{nl} = \varepsilon_0\chi^3\widehat{E^3}, \tag{A3}$$

$$\hat{J}_f = \frac{q_e^2}{m_e}\frac{\nu_c + i\omega}{\nu_c^2 + \omega^2}\widehat{\rho E}, \tag{A4}$$

$$\hat{J}_a = K\hbar\omega_0\widehat{\frac{\partial\rho}{\partial t}\frac{1}{E}}, \tag{A5}$$

where $\widehat{\ }$ denotes the spatiotemporal spectrum, ε_0 is the vacuum permittivity, $\chi^3 = 4n_0^2\varepsilon_0 c_0 n_2/3$ is the cubic susceptibility with n_2 being the nonlinear index, n_0 is the medium refractive index at the pulse central frequency ω_0, c_0 is the speed of light in vacuum, q_e and m_e are the charge and mass of the electron, ν_c is the collisions frequency, ρ is the concentration of free electrons (in $1/m^3$), and K is the order of the multiphoton ionization. The real part of $\hat{J}_f$ describes inverse Bremsstrahlung, and the imaginary part is responsible for plasma defocusing.

Together with the UPPE, we solve the kinetic equation for plasma concentration [27],

$$\frac{\partial\rho}{\partial t} = R_1(\rho_{nt} - \rho) + R_2\rho, \tag{A6}$$

where ρ_{nt} is the concentration of neutral molecules, with R_1 and R_2 being the optical field and avalanche ionization rates. To calculate R_1, we use the Perelomov-Popov-Terentiev (PPT) formula [30], while R_2 is given by

$$R_2 = \sigma(\omega_0)\frac{E}{U_i}, \tag{A7}$$

with

$$\sigma(\omega_0) = \frac{q_e^2}{m_e}\frac{\nu_c}{\nu_c^2 + \omega_0^2},$$

being the inverse Bremsstrahlung cross section at the pulse central frequency ω_0, and U_i the ionization potential. For the calculation of $\partial\rho/\partial t$ in Eq. (A5), we use only the first term on the right-hand side of Eq. (A6).

With a two-color field (mixture of fundamental ω_0 and its second harmonic $2\omega_0$) as the initial condition for Eq. (A1), we obtain a nonzero residual current $J_f(t\to\infty)$. Part of this residual current oscillates at THz frequencies [31]. Since according to Eqs. (A1) and (A2) the current J_f is a source term in the wave equation, we obtain a self-consistent model of THz generation.

Real atmospheric air is a mixture of several gases, including CO_2. One of the CO_2 absorption bands is located at 4.3 μm, that is, in close proximity to the central wavelength of our 3.9 μm pulse. In order to take into account the influence of CO_2 gas, we use the following model for complex frequency-dependent refractive index of air $n = n' + in''$ [24]:

$$n(\omega) = n_{\mathrm{Peck}}(\omega) + n_{\mathrm{HITRAN}}(\omega). \tag{A8}$$

The real-valued refractive index $n_{\mathrm{Peck}}(\omega)$ is given in [32], while to calculate the complex refractive index $n_{\mathrm{HITRAN}} = n'_{\mathrm{HITRAN}} + in''_{\mathrm{HITRAN}}$, we use the data on spectral lines of atmospheric gases from the HITRAN database [28]. The imaginary part n''_{HITRAN} is recalculated from the absorption coefficient given in the database; then the real part n'_{HITRAN} is restored using the Kramers-Kronig relations. To study the influence of CO_2 resonances, we calculated n_{HITRAN} for two gas mixtures that represent dry air (i.e., air with zero relative humidity): the first one with CO_2 (0.04% of CO_2, 79.06% of N_2, 20.9% of O_2) and the second one without CO_2 (79.1% of N_2 and 20.9% of O_2). The spectral lines for both mixtures are calculated for a temperature of 296 K and pressure of 1 atm. In Fig. 7, we plot the real part n' of the refractive index n and absorption coefficient $k'' = n''\omega/c_0$ as functions of frequency $f = \omega/2\pi$ for both gas mixtures. One can see that

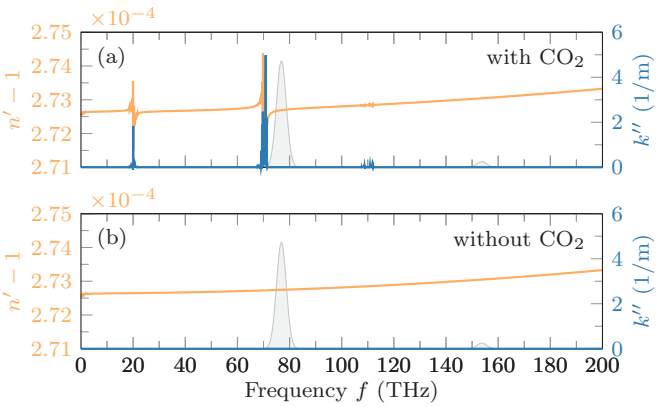

FIG. 7. The real part n' of the refractive index n [orange (light-gray) line] and the absorption coefficient [blue (dark-gray) line] vs frequency f for air (a) with and (b) without CO_2 gas. The spectrum of the initial 3.9 μm two-color laser pulse is marked by light-gray filling.

the presence of CO_2 gas in air gives rise to two absorption bands centered at 70 and 20 THz (4.3 μm and 15 μm, respectively). However, at this concentration of CO_2, the highest values of the absorption coefficient k'' do not exceed several inverse meters. Therefore, for our pulses focused by a 200 mm lens, we do not expect such strong influence of the linear absorption like in [24]. Nevertheless, the presence of CO_2 affects the sign of the second-order dispersion coefficient k_2 at $\lambda_0 = 3.9$ μm: for the gas mixture with CO_2, the $k_2 = -8.61 \times 10^{-29}$ s^2/m is negative and the dispersion is anomalous, while for the gas mixture without CO_2, the $k_2 = 4.18 \times 10^{-30}$ s^2/m is positive and the dispersion is normal.

In our simulations, we assume that the nonlinear index $n_2 = 10^{-23}$ m^2/W is the same for $\lambda_0 = 0.8$ and 3.9 μm (the corresponding values of critical power P_{cr} are 9.65 and 230 GW); the concentration of neutral molecules $\rho_{nt} = 2.5 \times 10^{25}$ 1/m^3, and collision frequency $\nu_c = 5 \times 10^{12}$ 1/s. To calculate the concentration of free electrons, ρ, we assumed that air consists of 79.1% of N_2 and 20.9% of O_2 molecules, with ionization potentials equal to 15.576 and 12.063 eV, respectively. For each molecule, we solved a separate kinetic equation.

We solved Eq. (A1) on an axially symmetric grid with the following parameters: the grid size and number of points in spatial domain are 10 mm and 1000, respectively (spatial resolution is 10 μm); the grid size and number of points in time domain are 10 ps and 65 536, respectively (the temporal and spectral resolutions are 0.15 fs and 0.1 THz).

[1] X. C. Zhang, A. Shkurinov, and Y. Zhang, Nat. Photon. **11**, 16 (2017).
[2] M. Tonouchi, Nat. Photon. **1**, 97 (2007).
[3] R. A. Lewis, J. Phys. D **47**, 374001 (2014).
[4] K. Reimann, Rep. Prog. Phys. **70**, 1597 (2007).
[5] W. R. Huang, S.-W. Huang, E. Granados, K. Ravi, K.-H. Hong, L. E. Zapata, and F. X. Kärtner, J. Mod. Opt. **62**, 1486 (2014).
[6] C. Vicario, A. V. Ovchinnikov, S. I. Ashitkov, M. B. Agranat, V. E. Fortov, and C. P. Hauri, Opt. Lett. **39**, 6632 (2014).
[7] J. A. Fülöp, Z. Ollmann, C. Lombosi, C. Skrobol, S. Klingebiel, L. Pálfalvi, F. Krausz, S. Karsch, and J. Hebling, Opt. Express **22**, 20155 (2014).
[8] M. Shalaby and C. P. Hauri, Nat. Commun. **6**, 5976 (2015).
[9] K. Y. Kim, A. J. Taylor, J. H. Glownia, and G. Rodriguez, Nat. Photon. **2**, 605 (2008).
[10] T. I. Oh, Y. J. Yoo, Y. S. You, and K. Y. Kim, Appl. Phys. Lett. **105**, 041103 (2014).
[11] D. Kuk, Y. J. Yoo, E. W. Rosenthal, N. Jhajj, H. M. Milchberg, and K. Y. Kim, Appl. Phys. Lett. **108**, 121106 (2016).
[12] I. Dey, K. Jana, V. Y. Fedorov, A. D. Koulouklidis, A. Mondal, M. Shaikh, D. Sarkar, A. D. Lad, S. Tzortzakis, A. Couairon, and G. R. Kumar, Nat. Commun. **8**, 1184 (2017).
[13] T. J. Wang, S. Yuan, Y. Chen, J. F. Daigle, C. Marceau, F. Théberge, M. Châteauneuf, J. Dubois, and S. L. Chin, Appl. Phys. Lett. **97**, 111108 (2010).
[14] T. J. Wang, J. F. Daigle, S. Yuan, F. Théberge, M. Châteauneuf, J. Dubois, G. Roy, H. Zeng, and S. L. Chin, Phys. Rev. A **83**, 053801 (2011).
[15] J.-F. Daigle, F. Théberge, M. Henriksson, T.-J. J. Wang, S. Yuan, M. Châteauneuf, J. Dubois, M. Piché, and S. L. Chin, Opt. Express **20**, 6825 (2012).
[16] K. Liu, A. D. Koulouklidis, D. G. Papazoglou, S. Tzortzakis, and X.-C. Zhang, Optica **3**, 605 (2016).
[17] M. Clerici, M. Peccianti, B. E. Schmidt, L. Caspani, M. Shalaby, M. Giguère, A. Lotti, A. Couairon, F. Légaré, T. Ozaki, D. Faccio, and R. Morandotti, Phys. Rev. Lett. **110**, 253901 (2013).
[18] W.-M. Wang, S. Kawata, Z.-M. Sheng, Y.-T. Li, L.-M. Chen, L.-J. Qian, and J. Zhang, Opt. Lett. **36**, 2608 (2011).
[19] A. V. Mitrofanov, A. A. Voronin, D. A. Sidorov-Biryukov, A. Pugžlys, E. A. Stepanov, G. Andriukaitis, T. Flöry, S. Ališauskas, A. B. Fedotov, A. Baltuška, and A. M. Zheltikov, Sci. Rep. **5**, 8368 (2015).
[20] P. Panagiotopoulos, P. Whalen, M. Kolesik, and J. V. Moloney, Nat. Photon. **9**, 543 (2015).
[21] A. V. Mitrofanov, A. A. Voronin, D. A. Sidorov-Biryukov, S. I. Mitryukovsky, A. B. Fedotov, E. E. Serebryannikov, D. V. Meshchankin, V. Shumakova, S. Alisauskas, A. Pugžlys, V. Y. Panchenko, A. Baltuška, and A. M. Zheltikov, Optica **3**, 299 (2016).
[22] A. V. Mitrofanov, A. A. Voronin, D. A. Sidorov-Biryukov, S. I. Mitryukovsky, M. V. Rozhko, A. Pugzlys, A. B. Fedotov, V. Y. Panchenko, A. Baltuska, and A. M. Zheltikov, Opt. Lett. **41**, 3479 (2016).
[23] P. Panagiotopoulos, M. Kolesik, and J. V. Moloney, Phys. Rev. A **94**, 033852 (2016).
[24] N. A. Panov, D. E. Shipilo, V. A. Andreeva, O. G. Kosareva, A. M. Saletsky, H. Xu, and P. Polynkin, Phys. Rev. A **94**, 041801 (2016).
[25] M. Kolesik, J. V. Moloney, and M. Mlejnek, Phys. Rev. Lett. **89**, 283902 (2002).
[26] M. Kolesik and J. V. Moloney, Phys. Rev. E **70**, 036604 (2004).
[27] A. Couairon, E. Brambilla, T. Corti, D. Majus, O. Ramírez-Góngora, and M. Kolesik, Eur. Phys. J.: Spec. Top. **199**, 5 (2011).
[28] "HITRAN on the Web", http://hitran.iao.ru/ (unpublished).
[29] L. A. Johnson, J. P. Palastro, T. M. Antonsen, and K. Y. Kim, Phys. Rev. A **88**, 063804 (2013).
[30] A. M. Perelomov, V. S. Popov, and M. V. Terent'ev, Sov. Phys. JETP **24**, 207 (1967).
[31] K.-Y. Kim, J. H. Glownia, A. J. Taylor, and G. Rodriguez, Opt. Express **15**, 4577 (2007).
[32] E. R. Peck and K. Reeder, J. Opt. Soc. Am. **62**, 958 (1972).